

STATISTICAL TRACING OF MAGNETIC FIELDS: COMPARING AND IMPROVING THE TECHNIQUES

KA HO YUEN¹, JUNDA CHEN^{1,2}, YUE HU^{1,3}, KA WAI HO⁴, A. LAZARIAN¹, VICTOR LAZARIAN¹ BO YANG¹
BLAKESLEY BURKHART⁵, CAIO CORREIA⁷, JUNGYEON CHO⁶, BRUNO CANTO⁷, J. R. DE MEDEIROS⁷

¹Department of Astronomy, University of Wisconsin-Madison, Madison, WI, USA

²Department of Computer Science, University of Wisconsin-Madison, Madison, WI, USA

³College of Electronics and Information Engineering, Tongji University, Shanghai, China

⁴Department of Physics, The Chinese University of Hong Kong, Hong Kong

⁵Smithsonian Center for Astrophysics (CfA), Harvard University, Cambridge, MA, USA

⁶Department of Astronomy and Space Science, Chungnam National University, Daejeon, Korea

⁷Departamento de Física Teórica e Experimental, Universidade Federal do Rio Grande do Norte, Brazil

ABSTRACT

Magnetohydrodynamic(MHD) turbulence displays velocity anisotropies which reflect the direction of the magnetic field. This anisotropy has led to the development of a number of statistical techniques for studying magnetic fields in the interstellar medium. In this paper, we review and compare three techniques that use radio position-position-velocity data for determining magnetic field strength and morphology : the correlation function anisotropy (CFA), Principal Component Analysis of Anisotropies (PCAA), and the more recent Velocity Gradient Technique (VGT). We compare these three techniques and suggest improvements to the CFA and PCAA techniques to increase their accuracy and versatility. In particular, we suggest and successfully implement a much faster way of calculating non-periodic correlation functions for the CFA. We discuss possible improvements to the current implementation of the PCAA. We show the advantages of the VGT in terms of magnetic field tracing and stress the complementary nature with the other two techniques.

Keywords: ISM:structure — magnetohydrodynamics (MHD) — methods: numerical

1. INTRODUCTION

Turbulence is an ubiquitous phenomenon in astrophysics (see [Draine 2009](#)) and it has been detected in the ISM ranges from kilo-parsecs to sub-AU scales ([Armstrong et al. 1995](#); [Elmegreen & Scalo 2004](#)) and responsible for the non-thermal broadening of line emission ([Kainulainen & Tan 2013](#); [Correia et al. 2014](#)). It is a well established fact that the interstellar medium (ISM) is turbulent and magnetized ([Padoan et al. 2004](#); [Burkhart et al. 2010](#); [Federrath et al. 2011](#); [Vázquez-Semadeni et al. 2011](#), see [Mac Low & Klessen 2004](#); [McKee & Ostriker 2007](#) for reviews). Magnetic turbulence controls a number of key astrophysical processes, e.g. cosmic ray propagation (see [Schleicher et al. 2010](#)), heat transfer ([Narayan & Medvedev 2001](#); [Lazarian 2006](#)) and transfer of polarized radio emission ([Draine 2005](#); [Haverkorn et al. 2006](#)). Moreover, ISM turbulence and magnetic fields are key components of the star formation paradigm ([McKee & Ostriker 2007](#); [Padoan et al. 2004](#); [Bialy et al. 2017b](#); [Burkhart 2018](#)). Scientists have known for decades, for example, that magnetic fields can control the collapse of molecular clouds ([Mestel & Spitzer 1956](#); [Spitzer 1978](#); [Shu 1983](#); [Mouschovias 1991](#)) and remove angular momentum from accretion disks (see [Krasnopolsky et](#)

[al. 2012](#)). More recently, magnetic turbulence has been identified as a driver of magnetic field diffusion from collapsing clouds and accretion disks via the process termed "reconnection diffusion" (see [Lazarian et al. 2012](#); [Mocz et al. 2017](#)).

The importance of magnetic fields and turbulence has resulted in the development of a number of techniques for studying these phenomena in observations. In general, there exist observational techniques (e.g. polarization or Zeeman studies) in the radio to optical wavelengths to study interstellar magnetic fields (see [Crutcher 2012](#) for a review). Techniques based on the statistical imprints of turbulence/gravity have also been suggested and employed ([Heyer et al. 2008](#); [Lazarian 2009](#); [Burkhart et al. 2017](#), see the thesis [Burkhart 2014](#) for a review). Suggested by the aforementioned statistical works, observational studies should use the feature of turbulence anisotropy when tracing magnetic field directions, e.g. the turbulence anisotropy measured in M51 using the method of correlation function from polarized synchrotron data ([Houde et. al 2013](#)). This opens up a radically new way to study magnetic fields than the traditional polarization or Zeeman studies.

MHD turbulence has been explored both theoretically and numerically (see [Shebalin et al. 1983](#); [Higdon 1984](#); [Montgomery & Matthaeus 1995](#). In the present-day, the theoretic-

cal foundations of magnetic field tracing techniques through turbulence statistics are based on the well-known theory proposed by Goldreich & Sridhar (GS95, 1995). They developed a theory for strong, incompressible, MHD turbulence that provides definitive predictions of the energy spectrum and anisotropy of velocity fields. GS95 proposes that there is a critical balance between nonlinear interactions and wave propagation, such that the timescales to transfer energy along the two directions are comparable. For an energy-conserving cascade, GS95 implies:

$$L_{\parallel} \propto L_{\perp}^{\frac{2}{3}} \quad (1)$$

The above relation is not available in the global system of reference. Therefore one should not expect the anisotropic relation can be observed in the global system of reference. The theory of turbulent reconnection (Lazarian & Vishniac 1999) has demonstrated the deep relationship and interdependence between MHD turbulence and magnetic field dynamics. The framework of Lazarian & Vishniac (1999) allows one to understand why, unlike the original GS95 treatment, the anisotropy of turbulence reflects not the mean magnetic field direction, but the direction of magnetic field that percolates turbulent eddies. Indeed, the turbulent reconnection theory predicts that magnetic field lines reconnect so fast that eddies are not constrained by magnetic field if they perpendicularly mix in the direction of the magnetic field of the eddy. This result was confirmed by numerical simulations (Cho & Vishniac 2000; Maron & Goldreich 2001; Cho & Lazarian 2003) and suggested that the study of anisotropy not only can define the mean magnetic field directions, but can also trace local variations of magnetic field direction.

The first suggestion to study magnetic fields statistically using the theoretical understanding of GS95 was the correlation function analysis (CFA) of the velocities (Lazarian et al. 2002; Esquivel & Lazarian 2011; Burkhart et al. 2014). In the aforementioned papers, the CFA analysis was applied to velocity channel maps obtained from MHD simulations¹. It was also demonstrated that the velocity anisotropies can indeed provide the direction of the mean magnetic field. In Esquivel & Lazarian (2005) and Esquivel et al. (2007) the CFA was quantified and elaborated. The technique was further explored as a way not only to find magnetic field direction, but also to determine magnetization (Esquivel & Lazarian 2011; Esquivel et al. 2015) as well as to determine the contribution of the fast, slow and Alfvén modes in observed turbulence (Kandel et al. 2016, 2017a,b).

The Principal Component Analysis of Anisotropies (PCAA)² provides another way of tracing magnetic field us-

ing the turbulence anisotropy (Heyer et al. 2008). The PCAA was successfully applied to the observations and shown to correspond to the polarimetry data (Heyer et al. 2008), as well the directions that were obtained with the technique.

Finally, the latest statistical technique for magnetic field studies, the Velocity Gradient Technique (VGT), was demonstrated as a tool to trace magnetic fields in interstellar medium and molecular clouds. The first work (González-Casanova & Lazarian 2017) on VGT used the velocity centroid gradients (VCGs) to trace magnetic field. Only approximate tracing was available and the accuracy of the technique was resolution dependent. A radical improvement of the VGT was achieved in Yuen & Lazarian (2017a), where the procedure of block averaging was used to provide reliable magnetic field tracing. The further development of the VGT for centroids was done in Yuen & Lazarian (2017b) suggesting that removing some wavemodes can improve the accuracy of magnetic field tracing. Another branch of the VGT, namely, Velocity Channel Gradients (VChGs) was developed in Lazarian & Yuen (2018a). The gradients of intensity fluctuations in thin channel maps were used to represent velocity fluctuations (see Lazarian & Pogossyan 2000). In the same paper (Lazarian & Yuen 2018a) suggested to use the galactic rotation curve in order to obtain the 3D distribution of magnetic fields. With the numerical studies of velocity gradients in self-absorbing media (González-Casanova et al. 2017) and application of the VCGs and VChGs to observed neutral Hydrogen (HI) and molecular tracer maps (Yuen & Lazarian 2017a,b; Lazarian & Yuen 2018a) the VGT was identified as a powerful new approach to tracing magnetic fields.

While all these three techniques appeal to GS95 as their foundation, it is not yet clear whether their predictions of magnetic field directions are in agreement with each other. Common questions of comparing these three field-tracing techniques would be: (1) *What are the constraints of the techniques?* (2) *How precise can we trace the B-field?* (3) *Are the methods self-consistent?*. In short, a benchmark study of all three methods in the same framework has yet to be performed. Yuen & Lazarian (2017a) first showed that VGT is superior over the CFA technique in tracing magnetic fields in observational data. This result has also been verified on a parallel work using the gradients of Synchrotron Intensities (Lazarian et al. 2017). They point out that, compared to VGT, CFA requires a larger area to perform the ensemble average in calculating the correlation function. The empirical nature of PCAA also brings questions to its applicability, i.e., there is no self-consistent check for whether PCAA is working in a certain region. VGT shows that having a number of 20^2 samples is sufficient to satisfy the Gaussian condition showed in

¹ Fluctuations of the intensity in so-called "thin velocity channel maps" are mostly influenced by velocity fluctuations, which the meaning of "thin channel" is quantified in Lazarian & Pogossyan (2000).

² We use PCAA to distinguish this analysis from the earlier studies in

Brunt & Heyer (2002b) where they used the Principal Component Analysis (PCA) to get the spectral indices of turbulence.

Yuen & Lazarian (2017a,b).

This paper aims to compare the three techniques and quantify their ability to trace magnetic fields (equivalently, detecting anisotropy) using synthetic maps generated from numerical simulations. As PCAA is not applicable to studying anisotropy in individual channels, we do not show the results of the VChGs analysis, although this technique provides the best tracing of magnetic fields among the different versions of the VGT. We investigate the advantages, limitations and constraints of these methods. We organize the paper as follows: In §2 we describe the details and properties of the simulations. In §3 we introduce the three methods of tracing magnetic field in detail. In §4 we show the result of comparison and in §5 we present a discussion of the results. We conclude our paper in §6

2. SYNTHETIC DATA FROM MHD TURBULENCE SIMULATIONS

The numerical data that we analyzed in this work is obtained by 3D MHD simulations using a single fluid, operator-split, staggered grid MHD Eulerian code ZEUS-MP/3D (Hayes et al. 2006) to set up a three-dimensional, uniform, and isothermal turbulent medium. Periodic boundary conditions are applied to emulate a part of the interstellar cloud. Solenoidal turbulence injections are employed. Our simulations employ various Alfvénic Mach numbers $M_A = V_L/V_A$ and sonic Mach numbers $M_S = V_L/V_S$, where V_L represents the injection velocity, V_A the Alfvén velocities, V_S the sonic velocity. All the cubes related to this work are listed in Table 1. The ranges of M_S , M_A and $\beta = 2M_A^2/M_S^2$ are specifically selected so that they cover different possible scenarios of astrophysical turbulence from subsonic to supersonic cases. However, limited by the turbulence scaling (See LV99), we devote most of our research to the sub-Alfvénic and trans-Alfvénic cases in this study.

To reduce the complexity of comparing the three methods, we only consider the optically thin case and synthesize observational maps using the following treatment. We first compute the PPV cubes from 3D numerical simulations. A PPV cube corresponds to a three-dimensional array with size n_x, n_y, n_v , where n_x, n_y represents the sizes along x and y axes, and n_v the number of velocity channels along the spectral line direction v (line of sight, LOS). The number of velocity channels is an adjustable parameter, and in our simulation, we choose $n_v = 400$ for our simulation and observation. The **Velocity Centroid** map $C(x, y)$ is a map weighted by velocity channel speed and has the size of $n_x \times n_y$. It is obtained by multiplying each velocity channel by its velocity, and then integrating along the velocity direction, and dividing by the total emission on the direction of integration:

$$C(x, y) = \Gamma^{-1}(x, y) \int dv v \rho(x, y, v) \quad (2)$$

where I represents the *integrated* intensity of the spectro-

Model	M_S	M_A	$\beta = 2M_A^2/M_S^2$	Resolution
Ms0.4Ma0.04	0.41	0.04	0.02	480 ³
Ms0.8Ma0.08	0.92	0.09	0.02	480 ³
Ms1.6Ma0.16	1.95	0.18	0.02	480 ³
Ms3.2Ma0.32	3.88	0.35	0.02	480 ³
Ms6.4Ma0.64	7.14	0.66	0.02	480 ³
Ms0.4Ma0.132	0.47	0.15	0.2178	480 ³
Ms0.8Ma0.264	0.98	0.32	0.2178	480 ³
Ms1.6Ma0.528	1.92	0.59	0.2178	480 ³
Ms0.4Ma0.4	0.48	0.48	2	480 ³
Ms0.8Ma0.8	0.93	0.94	2	480 ³
Ms0.132Ma0.4	0.16	0.49	18.3654	480 ³
Ms0.264Ma0.8	0.34	1.11	18.3654	480 ³
Ms0.04Ma0.4	0.05	0.52	200	480 ³
Ms0.08Ma0.8	0.10	1.08	200	480 ³

Table 1. Description of the MHD simulation cubes. M_S and M_A are the instantaneous values at each the snapshots are taken.

scopic cube, and ρ is the density of PPV cube:

$$I(x, y) = \int dv \rho(x, y, v) \quad (3)$$

In our implementations for the three methods below, most of our calculations are based on either the velocity centroid $C(x, y)$ ³ or the $\rho(x, y, v)$ (henceforth ρ when the meaning is clear in the context).

The orientation of anisotropy/gradients from the three methods are compared with synthetic polarization assuming a constant emissivity dust grain alignment process. In other words, the Stokes parameters $Q(x, y)$ and $U(x, y)$ can be expressed in terms of the angle θ between the y and z direction magnetic fields by $\tan \theta(x, y, z) = B_y(x, y, z)/B_z(x, y, z)$:

$$Q(x, y) \propto \int dz \rho(x, y, z) \cos(2\theta(x, y, z)) \quad (4)$$

$$U(x, y) \propto \int dz \rho(x, y, z) \sin(2\theta(x, y, z)) \quad (5)$$

The dust polarized intensity $I_p = \sqrt{Q^2 + U^2}$ and angle $\Phi = 0.5 \text{atan}2(U/Q)$ are then defined correspondingly. The alignment between the prediction of magnetic field (CFA, PCAA, VGT) and projected magnetic field orientations (polarization angles) are quantified by the **Alignment Measure (AM)**, introduced in analogy with the grain alignment

³ We cannot use the latest version of VGT (e.g. Lazarian & Yuen 2018a, Hu et al. 2018) to compare with either CFA or PCAA. Since in Lazarian & Yuen (2018a) they are performing per-channel gradient studies. For PCAA, it has no ability to perform per-channel prediction of magnetic field. While for CFA only the linearly summed channel anisotropy (Esquivel et. al 2015) is studied instead of the per-channel study for gradients in Lazarian & Yuen 2018a. To have a fair comparison, we have to use the Yuen & Lazarian (2017a) version of VGT, which uses the full PPV cube information to compare with CFA and VGT.

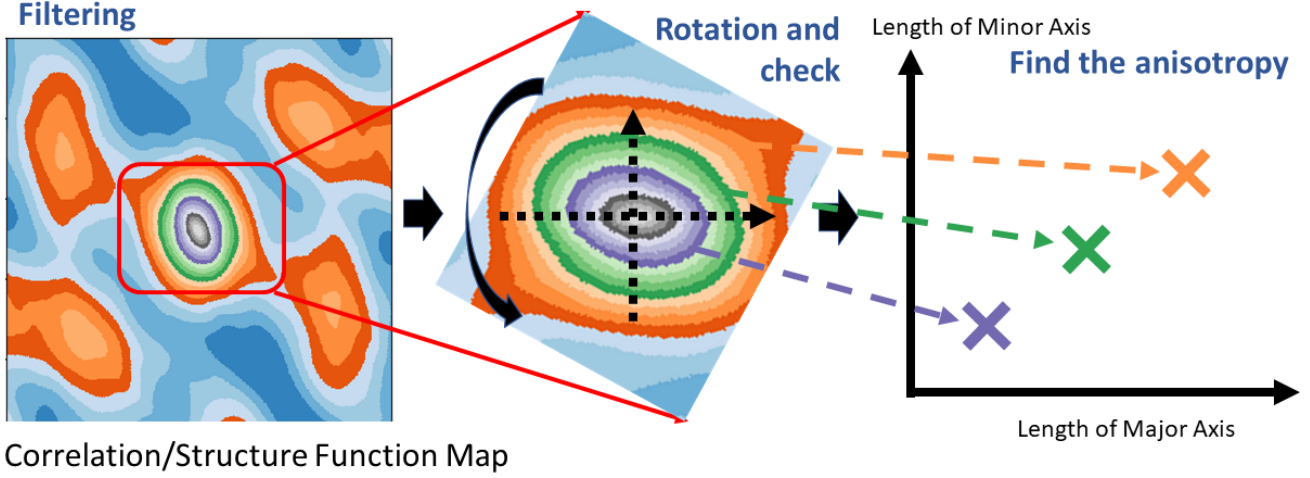


Figure 3. An illustration showing how the direction of anisotropy is detected using the rotation-detection algorithm. (Left) We first locate the region having elliptical contours and put the rotation center on the origin of the ellipses. (Middle) Then we slowly rotate the contours so that we identify the major and minor axes and both axes length are recorded for different contours. For example, the big dashed arrows shows the major and minor axes of the dark blue elliptical structure. (Right) The axes are then providing necessarily informations (direction, anisotropic length) for magnetic field studies.

decrease the time complexity of the computation process. We pad the centroid map C with size $n_x \times n_y$ (in Fig 2 $n_x = n_y = 3$) into two $(2n_x + 1) \times (2n_y + 1)$ block X, Y as shown in Fig. 2, where

$$X(i, j) = \begin{cases} C(\text{mod}(i-1, n_x)+1, \text{mod}(j-1, n_y)+1), & 1 \leq i, j \leq 2n \\ 0, & \text{otherwise} \end{cases} \quad (9)$$

$$Y(i, j) = \begin{cases} C(i, j), & 1 \leq i, j \leq n_x \\ 0, & \text{otherwise} \end{cases} \quad (10)$$

where mod is the modulo operation. The open-boundary correlation function is therefore

$$CF_C(\mathbf{R})[i, j] = \mathfrak{F}^{-1} \{ \mathfrak{F}\{X\} \mathfrak{F}\{Y\}^* \}, \quad 1 \leq i, j \leq n_x \quad (11)$$

This implementation enables one to compute the correlation function and structure function efficiently in non-periodic cases, which are particularly useful for our comparison between CFA and VGT.⁵ Figure 3 shows how to locate the direction of anisotropy given a specific correlation map or structure function map. Concretely, the algorithm plots the contour lines of the map, and detects the orientation of the elongated major-axes and minor-axes of each (elliptical) contour line. Then the map is rotated such that the major-axis of a contour with particular radius (in our case, the searching radius is 10 pixels) is parallel to the horizontal direction. The direction of anisotropy is then determined by the direction of major axis of the contour.

⁵ The Big-O factor for the Hockney's method is $O((2N+1)\log(2N+1))$ compared to the traditional method with $O(N^2)$, where N is the number of discrete elements in an array.

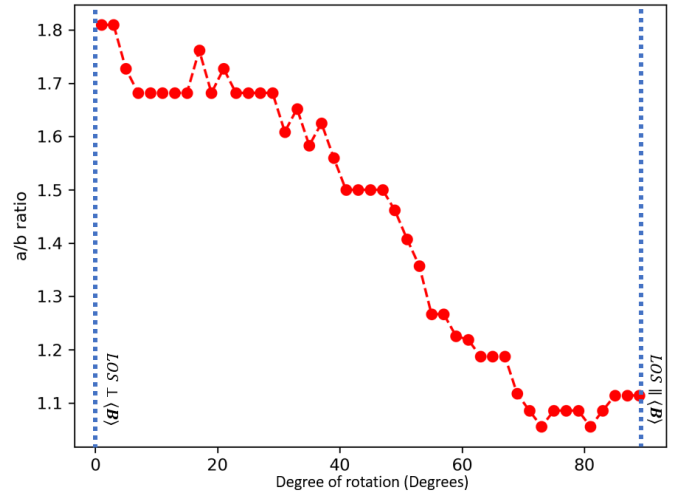


Figure 4. The change of a/b ratio with respect to the relative angle between the LOS and the mean magnetic field direction.

There are additional difficulties in using CFA when the line-of-sight makes a different angle to the mean magnetic field. [Burkhart et al. \(2014\)](#) suggested that the detected degree of anisotropy will drop when the angle between the line-of-sight to mean magnetic field decreases. We also see the same effect for our numerical cubes as in Fig 4. For VGT the respective investigation has been done in [Yuen & Lazarian \(2017b\)](#) and having similar drop of alignment measure when the angle between the line-of-sight to mean magnetic field decreases. However, observers should be aware of the fact that, while the degree of anisotropy is decreasing with respect to the decrease of angles between line of sight and the mean magnetic field, the predicted orientations are still evident for both VGT ([Yuen & Lazarian 2017b](#)) and CFA (Fig 4).

3.2. Analysis with PCA

3.2.1. Finding anisotropies with PCA

The PCA is widely used in image processing and image compression. In terms of astrophysical applications, the PCA analysis was used in [Brunt & Heyer \(2002a,b\)](#) for obtaining the turbulence spectrum from observations. In [Heyer et al. \(2008\)](#) the PCA was employed for studying turbulence anisotropies. The physical meaning of the eigenvalues from the PCA analysis are closely related to the value of the turbulence velocity dispersion v^2 . In particular, those larger eigenvalues correspond to the largest scale contributions of turbulence eddies along the line of sight $v^2 \sim (l^{1/3})^2 \sim l^{2/3}$, assuming GS95 scaling applies.

To study anisotropy, [Heyer et al. \(2008\)](#) applied the PCA to the spectroscopic data as a tool of tracing anisotropy, similar to what was done earlier in the statistical analysis of channel maps and centroids ([Lazarian et al. 2002](#); [Esquivel & Lazarian 2005](#)). Similar to the latter techniques, the directional PCAA demonstrated its ability to identify the direction of the mean magnetic field. To help the reader to understand the essence of the technique we provide a simple version of its mathematical formalism as well as a pictorial illustration in [Figure 5](#).

Assuming a proper normalization is used ⁶, we can treat the PPV cube $\rho(x, y, v)$ as the probability density function of three random variables x, y, v . The covariance matrix is:⁷

$$S(v_1, v_2) \propto \int dx dy \rho(x, y, v_1) \rho(x, y, v_2) \quad (12)$$

In the later treatment of anisotropy tracing, [Heyer et al. \(2008\)](#) splits the Position-Position-Velocity (PPV) cube into vertical and horizontal Position-Velocity tires (PV tires), where every PV tire is a vertical or horizontal slice from the PPV map $\rho(x, y, v)$ averaged over the x -direction (y -direction):

$$W(y, v) \propto \int dx \rho(x, y, v) \quad (13)$$

$$W(x, v) \propto \int dy \rho(x, y, v) \quad (14)$$

The covariance matrices (S_x and S_y) for the PV tires (W) are

$$S_x(v_1, v_2) \propto \int dx W(x, v_1) W(x, v_2) \quad (15)$$

$$S_y(v_1, v_2) \propto \int dy W(y, v_1) W(y, v_2) \quad (16)$$

⁶ In principle one shall use the normalized PPV cube $\rho' = \rho / \int \rho$. However for the treatment of PCAA, the difference of a constant does not alter the result. Therefore we stay with using ρ for simplicity.

⁷ The correct definition of covariance matrix should be $S(v_1, v_2) = E(\rho(v_1)\rho(v_2)) - E(\rho(v_1))E(\rho(v_2))$, where E is the expectation operator. However the second part was not included in [Heyer et al. \(2008\)](#)

hence eigenvalue equation for these covariance matrices are:

$$S_x \mathbf{u}_x = \lambda_x \mathbf{u}_x \quad (17)$$

$$S_y \mathbf{u}_y = \lambda_y \mathbf{u}_y \quad (18)$$

where the $\lambda_{\{x,y\},i}$ are the eigenvalues associated with the eigenvectors $\mathbf{u}_{\{x,y\},i}$ with $i = 1, 2, \dots, n_v$. The eigenvectors contain the information of velocity variations along this particular PV tire. To get information of the spacial variance, one must project each eigenvector into the PV tires. These eigen-projections, $P_{x,i}, P_{y,i}$ are:

$$P_{x,i}(x) = \int dv W(x, v) \mathbf{u}_{x,i}(v) \quad (19)$$

$$P_{y,i}(y) = \int dv W(y, v) \mathbf{u}_{y,i}(v) \quad (20)$$

With the sets of eigenvectors and eigen-projections on the x and y -direction in hands, one can apply the method of auto-correlation functions (ACFs) $ACF\{X\} = CF\{X\}/Var\{X\}$ to these sets of data in order to obtain the characteristic velocity and scale. Each characteristic velocity (scale) is calculated when the ACF for one eigenvector (eigen projection) drops by one e-fold. Due to resolution limitations, the characteristic velocities (scales) are interpolated between the nearest points to $1/e$:

$$\frac{ACF\{u\}(\delta v)}{ACF\{u\}(0)} = e^{-1} \quad (21)$$

$$\frac{ACF\{P\}(L)}{ACF\{P\}(0)} = e^{-1} \quad (22)$$

We obtain at least 10 pairs (See Right of [Fig 16](#)) of characteristic velocity $\delta v_{x,y}$, and scale $L_{x,y}$ from the ACFs of the correspondent eigenvectors and eigen projections.

If, as it is in the case of numerical data cubes, the magnetic field is oriented either along x or y axes, one can expect the ACFs for x and y -directions to be different. When using observational data, [Heyer et al. \(2008\)](#) attempted to find the direction of magnetic field by calculating the ACFs while rotating the directions of the x and y axes. This by itself can provide the magnetic field direction. However, [Heyer et al. \(2008\)](#) were studying the scaling of the ACFs while changing the orientation of the coordinate axes. The anisotropy was determined by the variations of the exponent α in:

$$\delta v_x = v_{0,x} L_x^{\alpha_x} \quad (23)$$

$$\delta v_y = v_{0,y} L_y^{\alpha_y} \quad (24)$$

An example can be found in [Fig 6](#). There are some challenges associated with this procedure. Indeed, according to both turbulence theory and MHD turbulence simulations (GS95, LV99, [Cho & Lazarian 2003](#)) the differences of indices should not be observed in the global system of reference related to the mean magnetic field. In the [Appendix B](#) we show that the observed differences between the indices are the result of both the limited inertial range of numerical

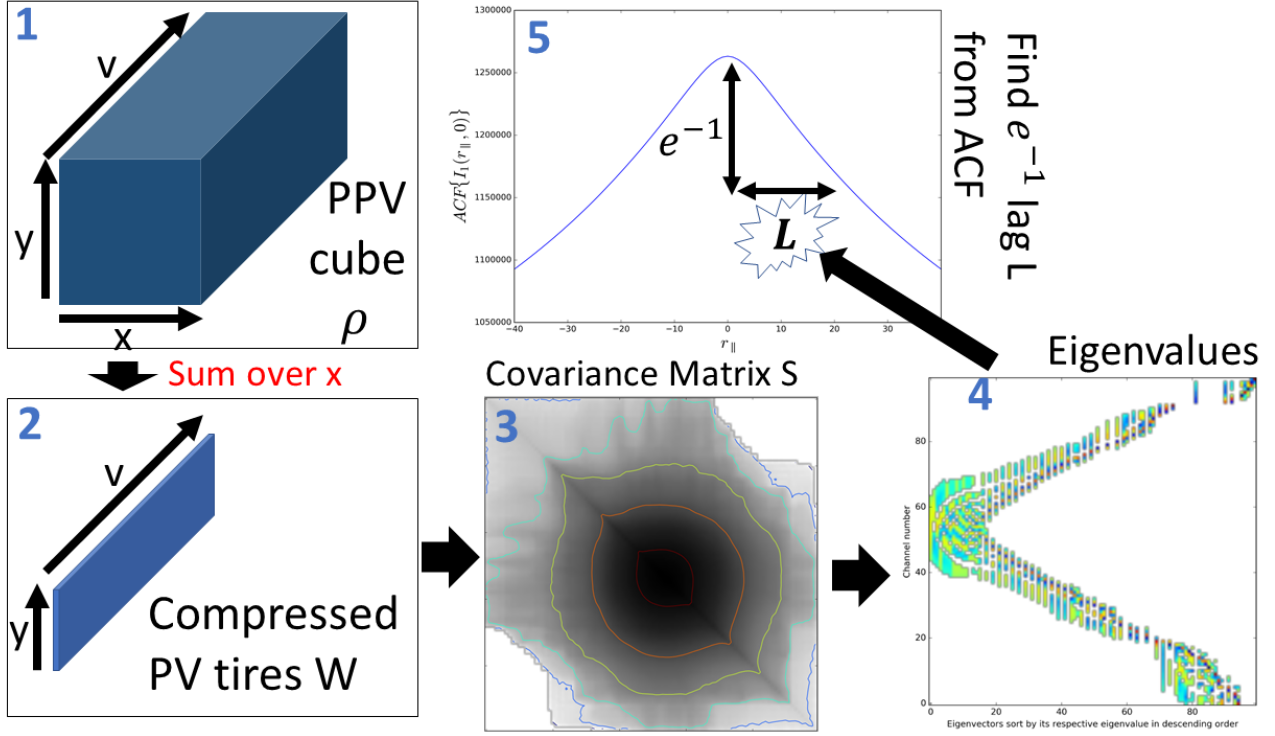


Figure 5. An illustration showing the pipelines of PCAA. We first project the PPV cubes along either of the spatial directions (panel 1), which we would call the compressed PPV cubes "PV tires" (panel 2) in which the covariance matrix S of the PV tires (panel 3, Eq. 15) can be computed. The eigenvalues of the covariance matrix (panel 4) contains the information velocity information along this particular PV tire, and the e^{-1} lag of the autocorrelation functions of the eigen-vectors and eigen-projections (panel 5, Eq. 21) tells the characteristic velocities $\delta v_{x,y}$, and length scales $L_{x,y}$ respectively.

simulations and the isotropic driving of turbulence at the injection scale.

While we find the approach in Heyer et al. (2008) has problems, for the sake of comparison, we use their formalism on the velocity and length-scale determinations (Eq. 21) as it is presented in their original work. In particular, we find the differences between the exponents α_x and α_y . Compared to the actual observational study in which the direction of magnetic field is not known a priori, a rotation of the coordinate system is required to *guess* the direction of magnetic field before applying PCA.⁸

3.2.2. Testing PCAA

We first prepare the PPV cubes with constant n and PPV density ρ by the distribution function of the line of sight ve-

⁸ The corresponding procedure is not elaborated in detail in Heyer et al. (2008). We feel that this procedure of rotating of the coordinate system is not straightforward in terms of its practical implementation. For instance, the calculation of the covariance matrix S_x for the PV tires (Eq. 15) requires an addition along the y -axis in the rotated coordinate. For both synthetic and observation maps, the information of the map is usually stored in a rectangular coordinate. Any kinds of addition after a rotation, as the PCA method did, will result in a distortion in the covariance matrix $S_{x,y}$

locity $f(v; z)$

$$n(x, y, v) = \int dz f(v; z) \quad (25)$$

$$\rho(x, y, v) = \int dz \rho(x, y, z) f(v; z) \quad (26)$$

We then apply the method of PCAA as illustrated. Fig. 6 shows how the density scaling in PPV cubes would change the anisotropies found by PCAA on the same numerical cube but with different weighting to density.

We also test our implementation of PCAA on our simulations as listed in Table 1. Fig 7 shows how the sonic Mach number M_s and Alfvénic Mach number M_A could possibly change the anisotropy. In this work we adopt an *isotropy* index which can be obtained directly from the PCAA exponents so we can compare to Velocity Centroids isotropy index,

$$\Upsilon = 1 - \frac{|\alpha_{\perp} - \alpha_{\parallel}|}{\sqrt{\alpha_{\perp} \alpha_{\parallel}}} \quad (27)$$

For isotropic velocity fields, $\Upsilon \sim 1$. Note that Υ can be negative for highly anisotropic clouds.

In Fig 7, we do not see a clear relationship between the isotropy index and M_s , but a slightly positive relationship between isotropy index and M_A is found. This is expected as in the PPV formulation using PCAA, only the largest vari-

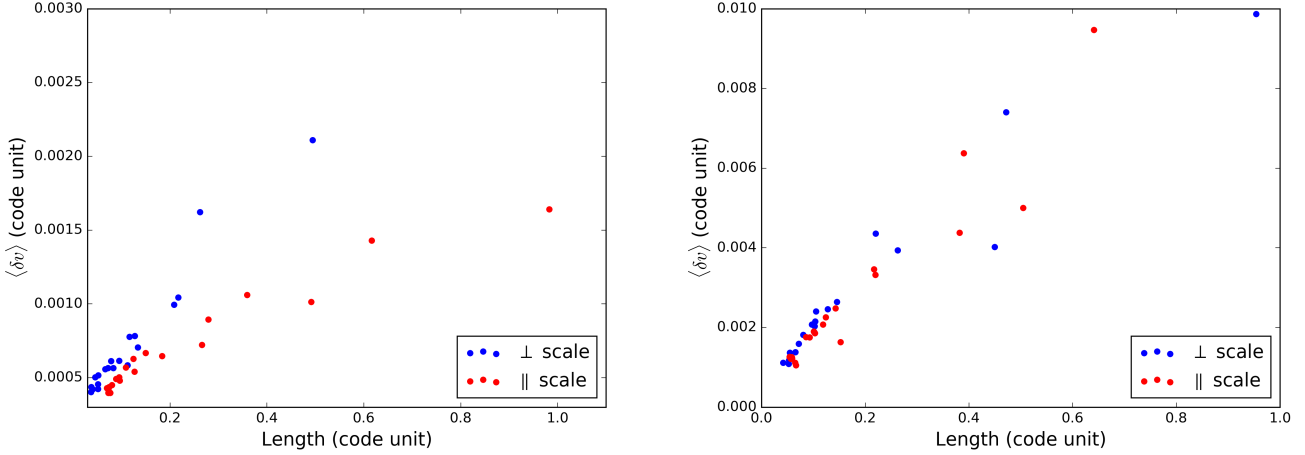


Figure 6. Two panels of scatter plots showing how the parallel and perpendicular pairs of $(\delta v, L)$ vary for the case when the PPV cube is constant-density (Left) or real-density (Right).

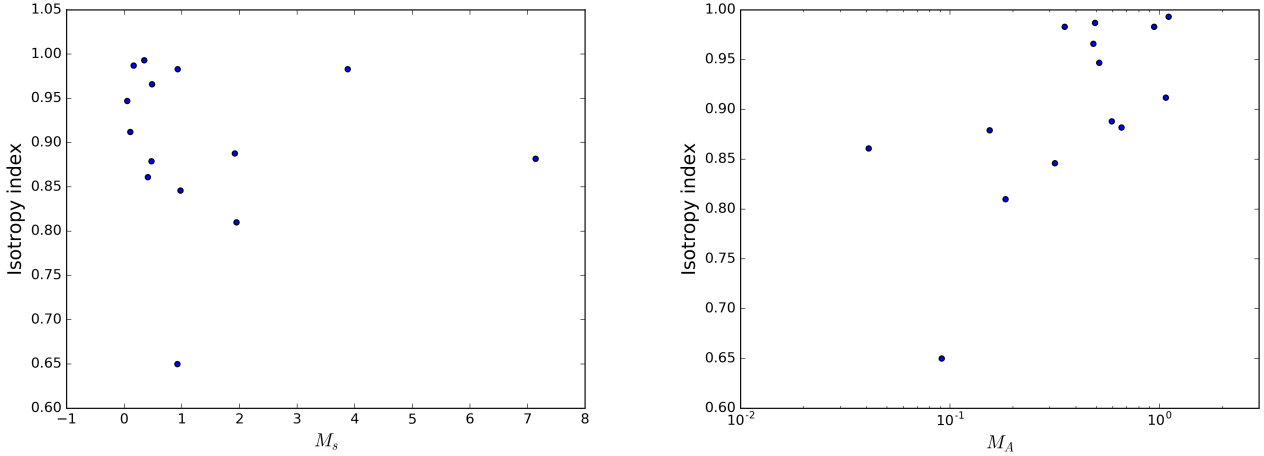


Figure 7. The plots show how the isotropy index (y-axis, see Eq (27)) varies with respect to M_s (Left figure, x-axis) and M_A (Right figure, x-axis)

ance contributions are extracted, and it is well known that the variance of density is a function of sonic Mach number $\sigma^2 \propto \log(1 + b^2 M_s^2)$ for some $b \sim 1/3 - 1/2$ (Federrath et al. 2011; Burkhart & Lazarian 2012). If as mentioned in the previous section only the largest eigenvalue is extracted, only the density clumps with the highest dispersion will, therefore, be analyzed.

We explained earlier that, in the global system of reference, there should not be a difference of the spectral indices based on the theory of MHD turbulence. To compare with VGT, which is a local measure of anisotropy, we have to improve the method of PCAA to the local scale instead of a global direction. In §4.2 we shall show our method of improving PCAA and compare with VGT.

3.3. The Velocity Gradient Technique

3.3.1. Block averaging

The Velocity Gradient Technique is a recently developed technique for tracing magnetic field directions based on the anisotropic turbulence scaling (GL17a, YL17a). In terms of the GS95 scaling, turbulent eddies are elongated along the local magnetic field directions. As a result, the gradients of velocity are perpendicular to the major axis of anisotropy, and thus the local magnetic field directions (See Fig. 8 for an illustration). In simple words, one can use the gradients of observables (e.g. Intensities I and Centroid C) to estimate the direction of magnetic fields by simply rotating the gradients by 90°

We adopt the sub-block averaging and the respective error-estimation method as suggested in YL17ab. While the gradients are good probes of magnetic field directions as suggested by our series of papers (Yuen & Lazarian 2017a,b; Lazarian & Yuen 2018a), knowing the errors of individual gradient vector is always beneficial when applying to observations. We have to emphasize on the basis of GS95 turbu-

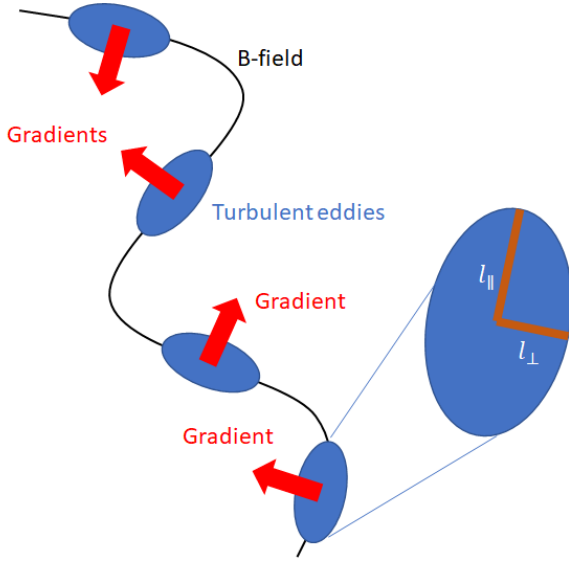


Figure 8. An illustration showing how VGT works. The MHD turbulent eddies (blue) are elongated along the local magnetic field (black line) directions. The gradients (red) of physical informations of these eddies (e.g. densities without shock influences, velocities, magnetic intensities) will therefore be maximally perpendicular to the local magnetic field directions. As a result, a simple 90° rotation of gradients trace the direction of magnetic field locally.

lence that the statistical nature of gradients acted similarly to the techniques based on turbulence anisotropy and principle component analysis (Esquivel & Lazarian 2005; Heyer et al. 2008; Burkhart et al. 2014). An insufficient number of pixels within the block will result in a significant error of magnetic field direction estimation. The recipe we proposed in YL17ab allows us to acquire the statistical gradient orientation average within a block from the peak value of the Gaussian fitting function $N(\theta; p_1, p_2, p_3) = p_1 \exp(-(\theta - p_2)^2 / p_3^2)$ in the gradient orientation distribution. The standard error of the Gaussian peak, δp_2 , which is one of the free parameters of the Gaussian function for fitting, will tell us how good the gradient orientation distribution follows the Gaussian distribution, and how accurate the peak can represent the *averaged* direction of gradients inside a particular block of certain size.

3.3.2. Recent Improvements for the VGT

Recently, it was demonstrated by Hu et al. (2018) that the method of Principal Component Analysis (PCA) is capable in extracting the anisotropic velocity modes along the line of sight. Different from the method of PCAA, Hu et al. (2018) construct the eigen-intensity maps I_{eigen} and eigen-centroid maps C_{eigen} using PCA as:

$$C_{eigen}(x, y) = \frac{\int dv \rho(x, y, v) \cdot v \cdot \lambda(v)}{I_{eigen}(x, y)} \quad (28)$$

$$I_{eigen}(x, y) = \int dv \rho(x, y, v) \cdot \lambda(v) \quad (29)$$

where the λ are the eigenvalues associated with the eigenvectors \mathbf{u} .

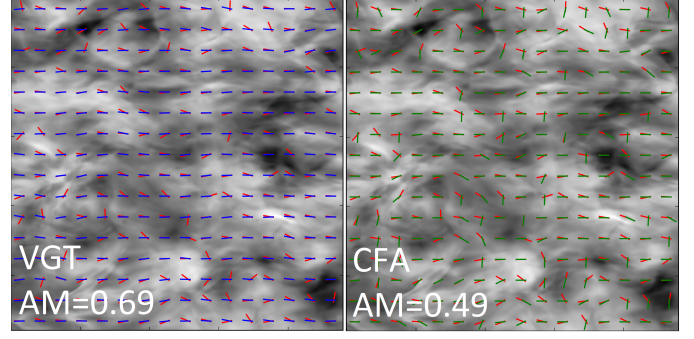


Figure 9. A plot showing the B-field orientation probed by VGT (red) and CFA (green) versus the magnetic field directions (blue) overlaid on the velocity centroid maps with both block size of 30 pixels on the cube with $M_s = 1.92$ & $M_A = 0.59$.

In both synthetic and observational maps, the extraction of eigen-centroids can effectively probe the direction of magnetic field with very high accuracy. As a result, for the studies of the projected magnetic field, the improved technique can provide higher accuracy of magnetic field tracing.

4. COMPARISON BETWEEN THE THREE TECHNIQUES

The common goal of the three methods (CFA, PCAA, VGT) is to trace magnetic field orientation independently from polarimetry measurements. For VGT, the accuracy of determining the magnetic field direction can be obtained through block averaging (Yuen & Lazarian 2017a; Lazarian & Yuen 2018a).⁹ The other two techniques have their limitations. For instance, the CFA technique depends strongly on the viewing angle chosen (Burkhart et al. 2014). We have not developed yet a self-consistent procedure for estimating the accuracy of the magnetic field orientation with CFA like the Gaussian fitting criterion in VGT sub-block averaging (Yuen & Lazarian 2017a). The PCAA technique in its present incarnation seems to have even more problems. The determination of the anisotropy angle using PCAA requires tedious checking of anisotropy index in *every* possible angle that the map can rotate. Moreover, the projection of PV tires after rotation will result into distortion of the PV tire statistics. As a result, the autocorrelation function may not provide the anisotropy direction correctly. Moreover, the perpendicular and parallel velocity scaling indices α are not expected to change for turbulence with extensive inertial range.

Nevertheless, the synergy of the techniques should be utilized. We note that an advantage of CFA is that, the related anisotropies are analytically described in Kandel et al. (2017a) and are related to the contributions from slow, fast

⁹ In our forthcoming paper we are comparing the VGT with tracing of filaments in channel maps that is suggested in Clark et al. (2014, 2015). We feel that the filaments in the latter papers are results of the velocity crowding, the same effect that makes thin channel maps sensitive to velocity fluctuations (Lazarian & Pogosyan 2000).

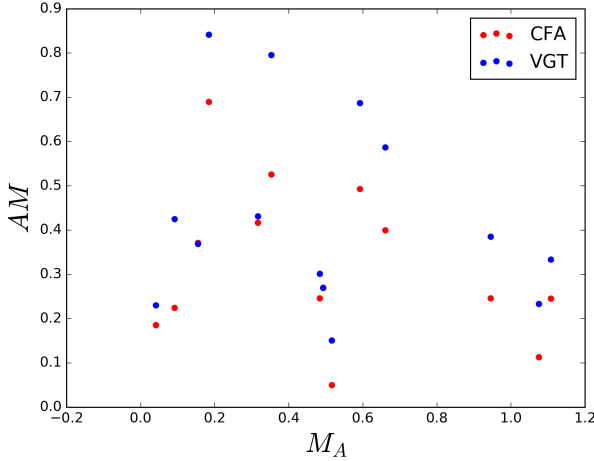


Figure 10. A scatter plot showing the AM of VGT (Blue) and CFA (Red) to B-field respectively against the Alfvénic Mach number M_A .

and Alfvén modes that constitute the MHD turbulence cascade (Cho & Lazarian 2003). Below we provide a more quantitative comparison of the 3 techniques.

4.1. VGT vs CFA

Fig. 9 shows a visual comparison of applying both VGT and CFA on the same centroid data from the Ms1.6Ma0.528 simulation by selecting a block size of 30 pixels. We compare the performance of CFA with the older VGT recipe (from Yuen & Lazarian 2017a), which the latter carries only one user-defined variable, the block size. For the B-field orientation probed by CFA, we use the orientation of the major axis as a prediction following the treatment in §3.1 (See Fig. 3). The algorithm suggested in §3.1 is more adaptive in dealing with irregular anisotropic shapes compared to our previous treatment in (Yuen & Lazarian 2017a) using a highly simplified gradient-at-origin for correlation function method¹⁰. We select the pixel distance of 10 pixels for anisotropy contour detection.

One can see a significant advantage of VGT compared to CFA in Fig. 9 in terms of the alignment measure. Figure 10 shows a scatter plot of AM_{VGT} to AM_{CFA} with respect to M_A using the gradient recipe of Yuen & Lazarian (2017a) for a block size of 30 pixels. The mean AM for VGT is ~ 0.43 while that for CFA is about ~ 0.31 . While we do not see a clear trend of $\Delta AM = AM_{VGT} - AM_{CFA}$ versus M_A , there is a general of $\Delta AM = 0.2$ advantage for VGT over CFA.

We do expect that the tracing power of VGT increase appreciably after the improvements suggested from Lazarian & Yuen (2018a). But whether we can use the same improve-

¹⁰ In principle, the shorter axis direction for the anisotropy corresponds to larger gradients. Therefore one can try to detect the anisotropy by taking gradients at the origin of correlation functions and rotate 90° for magnetic field directions. This, however, cannot tackle complex structures like what we see in Fig 15

ment technique for CFA-probed B-field is not clear yet. One can visually see from Fig 9 that the magnetic field estimations from CFA are more likely to be bi-model, i.e. the vectors are likely to be either parallel or perpendicular to the real field. This might due to the fact that small-scale statistical shape studies are not well studied (See Fig 15 for a pictorial illustration).

4.2. VGT vs PCAA

To compare PCAA with VGT, we update the implementations of PCAA to make it comparable to the sub-block averaged method in VGT. The general guideline would be *performing PCAA on sub-blocked PPV cubes*. We extract the partial PPV (pPPV) cubes ρ_{ij} that covers partial spatial regions:

$$\rho_{ij}(x, y, v) = \rho((i-1)n+x, (j-1)n+y, v) \quad (30)$$

The sequence of PPV cubes ρ_{ij} contains in total $n_x n_y / n^2$ elements. For each pPPV cube, we assume they are independent and processed using the steps from §3.2. One can refer to Figure 5 for the simplified, pictorial work flow for PCAA. The product from the pipeline would be a 6-element array $(\delta v_x, \delta v_y, L_x, L_y, \alpha_x, \alpha_y)_{ij}$ for each pPPV cube, which they should have an empirical scaling as shown in Eq (23) & (24).

One can try to convert the anisotropic direction predicted by PCAA in each PPV cube¹¹ to some magnetic field orientation prediction similar to VGT. The trick is to use the fact that the 6-element array provides a measure of velocity gradients, and the maximal-perpendicular properties of velocity gradients allow us to predict the direction of magnetic field by rotating PCA-backed velocity gradient by 90° . We start with the *statistical average* maximal PCAA-gradient orientation inside the block (i, j) assuming both L_x, L_y are small and not aligned with the \parallel, \perp coordinate

$$\nabla v(L_x, L_y) \sim \left\langle \frac{\delta v_x}{L_x}, \frac{\delta v_y}{L_y} \right\rangle \quad (31)$$

The orientation of PCAA gradient is then given by,

$$\tan \theta(L_x, L_y) = \frac{\delta v_y L_x}{\delta v_x L_y} = \frac{L_y^{\alpha_y-1}}{L_x^{\alpha_x-1}} \quad (32)$$

For L smaller than some turbulence scales depending on the Alfvénic Mach number (See LV99 for a complete discussion), i.e. L is sufficiently small, we can then obtain an expression from Eq 32 of approximating the PCAA angle:

$$\tan \theta = \frac{1 - \alpha_x}{1 - \alpha_y} \quad (33)$$

¹¹ This is, however, not a very accurate statement, as PCAA has a pre-assumed anisotropy direction. In Heyer et al. (2008) they illustrate how the anisotropy direction by rotating the Taurus map and see which orientation can give the largest anisotropy difference.

Fig. 11 shows how the magnetic field orientation predicted by $\theta + \pi/2$ from Eq. (33) is compared to polarization measurements and VGT. In the following, we discuss the two separate cases regarding properties of PPV cubes.

4.2.1. Constant Density Case

We first investigate how the block-averaging would behave in the constant density PPV cube (Burkhart et al. 2013). In other words, we create PPV cubes with a uniform density field and a turbulent velocity field. Thus all fluctuations in such a cube are entirely due to velocity caustics. On the left of Figure 11 shows how the performance of PCAA is compared to VCG visually in a centroid map from super-Alfvénic simulation Ms3.2Ma0.32. For some part of the region, PCAA is able to trace magnetic field accurately; however, the alignment measure for the PCAA-magnetic field is negative, which means the results from PCAA are almost perpendicular to magnetic field. Comparatively, VCG has an alignment measure almost close to one. This suggests that VCG is more accurate for tracing the direction of the magnetic field.

4.2.2. Real Density Case

We also explore how the use of real density PPV cube would change the alignment measure of VGT and PCAA. In theory the involvement of real density will make the velocity channel map contains both density and velocity contribution, in which the proportion among the two contribution is determined by the channel thickness (LP00) and also the sonic Mach Number. When we sum up the channels, density is expected to dominant over velocity contribution, and the alignment measure is expected to drop compare to the constant density case.

On the right of Fig 11 shows how the performance of PCA is compared to VCG visually in a centroid map from super-Alfvénic simulation Ms3.2Ma0.32. Comparing with the constant density case, the alignment of PCA is improved closing to zero. However, VCG still provides an excellent performance in tracing magnetic field, even through we do see a drop of alignment measure from the constant density case.

5. ADDITIONAL EFFECTS

5.1. Fluctuation of anisotropy scale and directions in CFA

The method of CFA has its limitations in both resolution and quality of the data, both to simulations and observations. In principle, numerical simulations have limited inertial ranges. In terms of correlation and structure functions, only the small-scale contributions are considered to be meaningful. This is also true for observation where bulk motions exist (e.g. galactic motions and shear, outflow) aside from turbulence. As a result, the large-scale part of the correlation function may not be so meaningful in determining the anisotropy. However, this immediately brings a paradox of

the anisotropy direction, as the small-scale part is often limited with only several pixels only and highly depends on the quality of the data.¹² If the resolution of the map is small (in observation) or the dissipation process is strong (in numerical studies), the small-scale anisotropy determination under the assumption of elliptical elongation would fail (See Sec 3.1 for the method building). The change of anisotropy is even more severe when the number of samples for the statistical studies is not enough (e.g. Sec 4.1). To what extent the correlation function anisotropy can provide a correct answer given a map with certain resolution is uncertain.

Model	M_S	M_A	$\beta = 2M_A^2/M_S^2$	Resolution
H0	7.36	0.22	0.0017	792^3
H1	6.41	0.41	0.0083	792^3
H2	6.47	0.61	0.0176	792^3
H3	6.47	0.80	0.0309	792^3
H4	6.15	1.00	0.0531	792^3

Table 2. Description of the MHD simulation cubes with larger resolution. M_S and M_A are the instantaneous values at each the snapshots are taken.

We therefore want to test the dependences of resolution to the anisotropy method using multiple resolutions. We prepared some higher resolution cubes (Table 2) and compare with what we have (Table 1) for both the anisotropy axis ratio and its orientation.

5.1.1. Distortion of anisotropy over scales

We first illustrate the effect of scale-dependent anisotropy in our numerical cube with lower resolution (480^3). Fig. 12 shows how the shape and orientation of the correlation function anisotropy in Ms0.4Ma0.04 is changing with respect to length. One can directly see that while the numerical cube is somewhat anisotropic in all scales visually, both the axis ratio and the orientation are changing when one steps away from the center of the ellipses. On the left of Fig. 13 shows a clearer effect with a scatter plot from three numerical simulations Ms0.4Ma0.04, Ms0.8Ma0.08 and Ms1.6Ma0.16, illustrating how the pixel distance (defined as the distance from the common center for the anisotropic ellipses) to the relative angle that the smallest anisotropy elongates to.

We can also try to quantify this effect with the major/minor axis ratio (a/b ratio). The right panel of Figure 13 shows how the a/b ratio varies with respect to the pixel distance in our three selected simulations Ms0.4Ma0.04, Ms0.8Ma0.08 and Ms1.6Ma0.16. We can see an unexpected effect regarding the

¹² While readers might challenge whether the large-scale shearing/rotation motion or the small-scale outflow motions may alter the result of VGT. In principle, with proper scale filtering Yuen & Lazarian (2017b) one can remove the contribution from large scale structures, which is also true for the method of CFA. For the small scale outflow motion using a large enough block size can average out the contribution of non-turbulent motions.

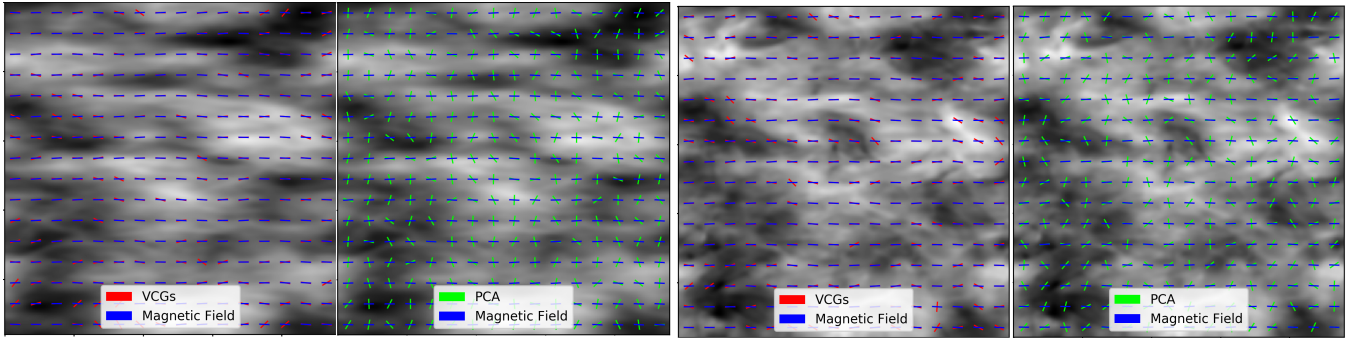


Figure 11. A comparison between the magnetic field predictions from VGT and PCAA when the constant density condition (first and second panel) and turbulent real density condition (third and fourth panels) are applied respectively. In the first two panels, the fluctuations are entirely due to velocity fluctuations, since the density is held constant. In this figure we use the Model Ms3.2Ma0.32. Block size=30.

A change of anisotropy direction as "radius" increases

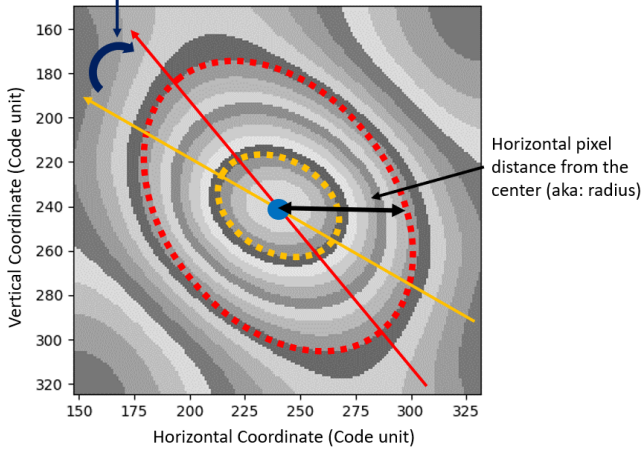


Figure 12. An illustrative figure showing how the direction of anisotropy changes with respect to contour size: A yellowish contour with "radius" (Defined in the figure as the horizontal pixel distance from the center) of ~ 20 is selected and the direction of anisotropy for this contour is shown by a yellow arrow. One can pick a bigger contour (e.g. the reddish one we picked with "radius" of ~ 60), the direction of anisotropy for this contour is changed significantly.

resolution: The smaller M_A is actually being less anisotropic! What if we increase the resolution and simulate cubes with appropriate M_A that its scale $L_{inj}M_A^2$ is within the inertial range. On Fig. 14 shows how the cubes from the same code with higher resolution would behave. One can see from the trend for a/b axis ratio and orientation oscillations are closer to theoretical expectations (Esquivel & Lazarian 2005), that a/b ratio is decreasing with respect to M_A , and orientation is more stable. This illustrates the resolution of the map is critical for the CFA study

5.1.2. Disappearance of elliptical anisotropy

The resolution problem not only can distort the shape of the anisotropies in different scales, but also destroy the prominent elliptical shape, especially when performing the sub-block CFA analysis (Eq 11). Figure 15 shows how the

shape of anisotropy is changed when one selects a different size of a partial region from the same cube Ms0.4Ma0.04. While the mean magnetic field stays pretty constant throughout the whole region, both the direction and the shape of contours change dramatically from elliptical to straight lines when one decreases the sampling size.

It is worth noting that some isocontours in Fig 15 show strip-like structures and, intuitively, the anisotropy is considered indeterminable in the region of interest. One possibility is that the measured region only contains small-scale turbulence in numerical box, which is contributed mostly from the dissipative ranges, so that the velocity motions in such a small region are similar to a noise-like environment. The effect of small area for CFA is similar to the uniform distribution for velocity gradient distribution we see in very small block size (Yuen & Lazarian 2017a), notifying that the samples (Both VGT and CFA) inside the region of interest is simply statistically not adequate for any kinds of anisotropy/magnetic field estimate. As the resolution decreases, the number of strip-like isocontours increases significantly, causing the result to be indeterminable for all scales of interest.

5.2. Dependence of channel resolution in PCA

While PCAA is a very powerful tool in extracting spectrum properties through a relatively simple statistical pipeline, there are concerns about its consistency and arbitrariness when applying to both synthetic and real observation. Two very important questions would be : 1. What is the minimal velocity channel number for PCAA and 2. What is the optimal number that one can pick for the ACF analysis? They are both crucial as how important a particular velocity spectral line eigenvector is depended on both the channel resolution and the number of biggest eigenvalues that are picked when fitting the α values.

We first illustrate how the channel resolution would change the answer of PCAA. The left figure of Fig.16 shows a relation of isotropy index to the channel resolution for both constant and real density PPV cubes (See Eq (25)) on the cube Ms1.6Ma0.528 by using 10 eigenvalues. One can see that

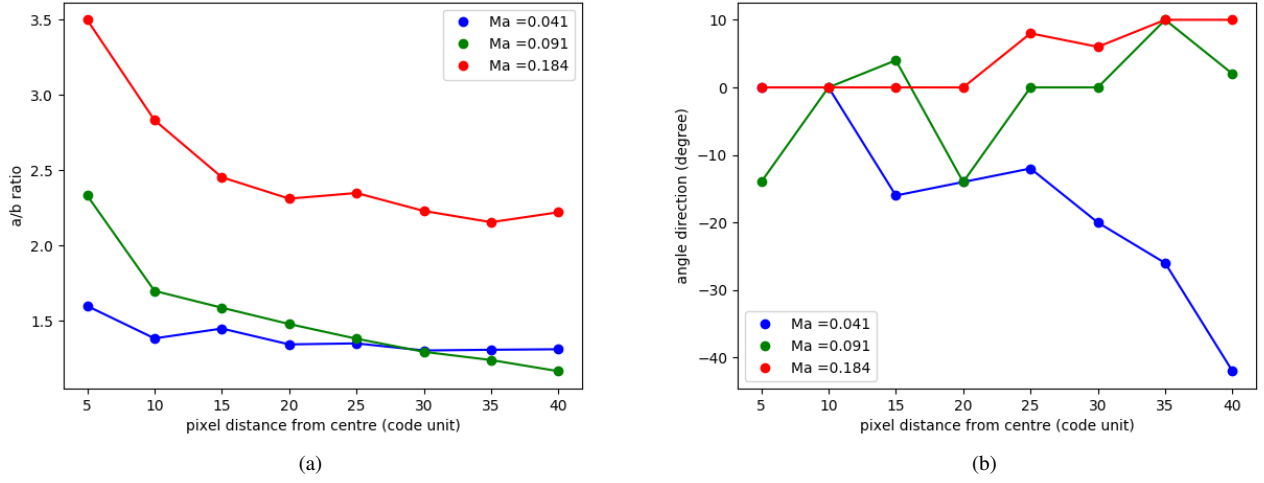


Figure 13. Showing two main properties of CFA to difference Ma under resolution 480^3 . Figure (a) shows the axis ratio to difference radius from the center. Figure (b) shows the variation degree difference to difference radius from the center.

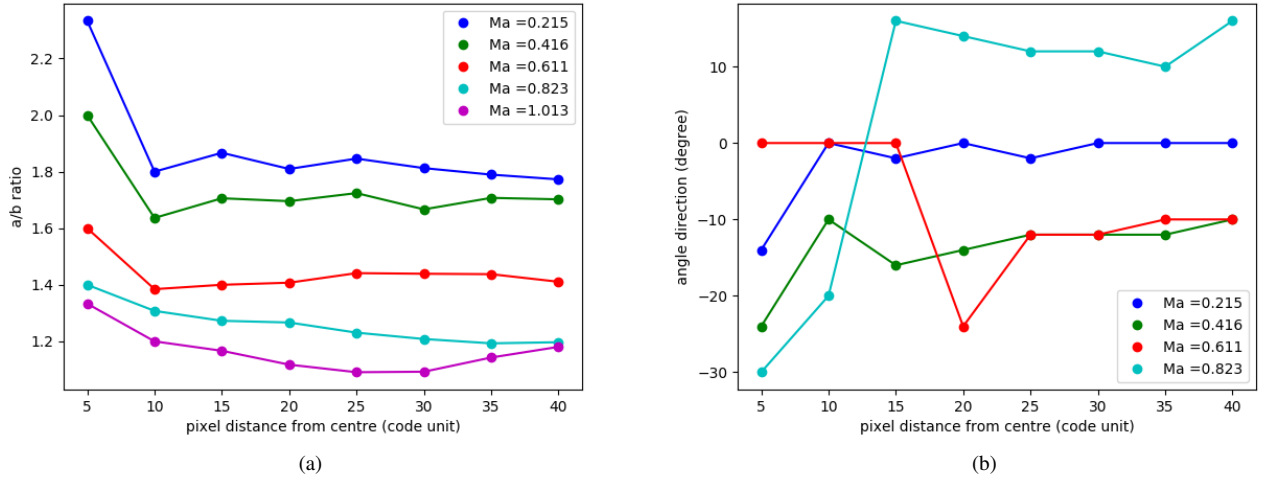


Figure 14. Showing two main properties of CFA to difference Ma under resolution 792^3 . Figure (a) shows the axis ratio to difference radius from the center. Figure b shows the variation degree difference to difference radius from the center.

the isotropy index fluctuates dramatically when the channel number is less than 200 pixels and stays constant afterward. This indicates the method of PCAA has a more significant error if the velocity channel resolution is not enough. In particular, our test shows an approximately 20% error for constant density case and 12% for real density case in terms of the isotropy index. If one converts the isotropy index back to the angle, a larger error is expected. In this test, we did not include the noise produced by the instruments (which is very common in observational spectroscopic cubes). However, due to the nature of PCAA pipeline, the noise only contributes to the velocity spectra modes with small eigenvalues.

We also test whether there is a way to search for the optimal number of principal components for PCAA analysis. In

previous literature, only a handy of modes are used in PCAA (e.g. Brunt & Heyer (2002b) used 8 modes, and Correia et al. (2016) use 3 to 12). We use a $n_v = 100$ cube to test how the change in the number of eigenvalues picked for PCAA would change the anisotropy measurement. Fig. 16 (right panel) shows the variation of isotropy index to the number of principal components we used for PCAA analysis, for both the actual turbulent density field (i.e. denoted as "real") and a constant density field. One can see a significantly larger variation when the number of principal components is smaller than 20. For instance, the isotropy index changes from 0.05 to 0.8 when the number of principal components changes from 5 to 15 for the real density case. Relatively, the constant density PPV cube is more robust when the number of

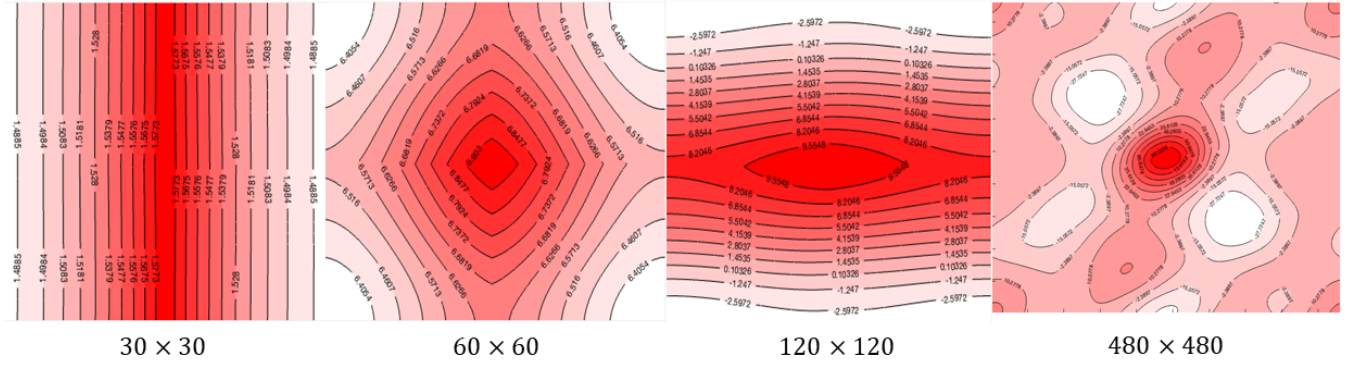


Figure 15. The variation of correlation function anisotropy shapes with respect to block size for the cube Ms0.4Ma0.04. We draw contours to specify the isocontours.

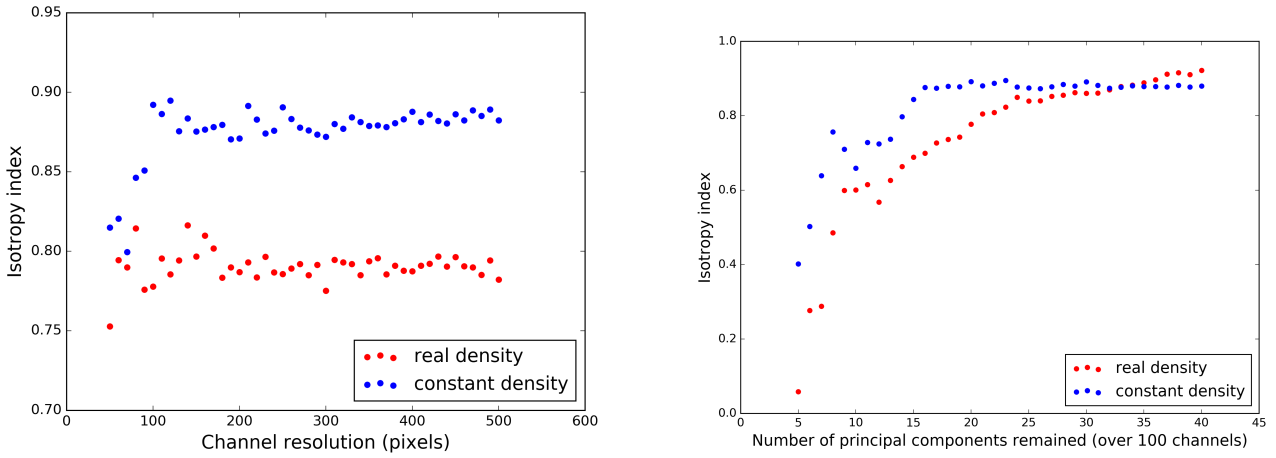


Figure 16. The plot shows how the isotropy index (y-axis) varies with respect to channel resolution (Left figure, x-axis) and the number of principal components remained (Right figure, x-axis).

principal components is changing, but the variation is still large until component 20.

One may argue whether the use of an intensity threshold for the higher eigen-projections may provide more stability to the isotropy index. However, the extra dependency on the intensity threshold will also increase the difficulty for observers to find the best combination of channel number, the number of components and the threshold value to analyze the result with PCAA.

6. SUMMARY

In this paper, we studied three different techniques that have been suggested in the literature for tracing magnetic field. We improved these techniques and compared them with each other. In particular, for the CFA technique we suggested and successfully tested a way of finding the direction of the magnetic field more accurately as well as a way of calculating correlation functions quickly. We also suggested the sub-block averaging technique for the PCAA. Our finding can be summarized as:

1. Velocity Gradient Technique is a more superior tech-

nique compared to CFA and PCAA in tracing magnetic fields.

2. Correlation Function Anisotropy faces several issues when the block size is small. In particular, the anisotropies may be distorted, multi-centered or the contours are not closed. That significantly affects the determination of the direction of anisotropy, thus magnetic field. Poor resolution may also hinder the CFA technique from correctly determining the Alfvén Mach number.
3. Principle Component Analysis provides a method for extracting the most important velocity components in a PPV map. However, the detection of anisotropy strongly depends on the quality of spectroscopic cubes and the number of components that are being analyzed. We report only a weak dependence on M_A and no dependence on M_S . With the block-averaging technique applied, we show that VGT has a significant advantage compared to PCA for finding magnetic field detections.

Acknowledgments The research activities of the Observational Astronomy Board at the Federal University of Rio Grande do Norte (UFRN) are supported by continuous grants from the Brazilian agencies CNPq and FAPERN and by the INCT-INEspaĂgo. B.L.C.M. acknowledges a PDE/CAPES fellowship. A.L. acknowledges the support the NSF grant DMS 1622353 and AST 1715754, a Distinguished Visiting Professor PVE/CAPES appointment at the Physics Graduate Program at UFRN, Natal, Brazil and a Visiting Professor Fel-

lowship of the UFRN. B.B. acknowledges support from the Institute for Theory and Computation (ITC) fellowship at the Harvard-Smithsonian Center for Astrophysics. We acknowledge Rachel and Vera for their kindly support of our numerical calculation. J.C.'s work is supported by the National Research Foundation of Korea Grants funded by the Korean Government (NRF-2016R1A5A1013277). We acknowledge Jeff Godsey from the Writing Center of UW-Madison for pointing language improvements on our paper.

Software: Julia, Matlab, Python

REFERENCES

- Armstrong, J. W., Rickett, B. J., & Spangler, S. R. 1995, *ApJ*, 443, 209
 Bertram, E., Shetty, R., Glover, S. C. O., et al. 2014, *MNRAS*, 440, 465
 Bialy, S., Burkhart, B., & Sternberg, A. 2017b, *ApJ*, 843, 92
 Brunt, C. M., & Heyer, M. H. 2002a, *ApJ*, 566, 276
 Brunt, C. M., & Heyer, M. H. 2002, *ApJ*, 566, 289
 Brunt, C. M., Heyer, M. H., Vázquez-Semadeni, E., & Pichardo, B. 2003, *ApJ*, 595, 824
 Burkhart, B., & Lazarian, A. 2012, *ApJL*, 755, L19
 Burkhart, B. K. 2014, Ph.D. Thesis,
 Burkhart, B., Lazarian, A., Goodman, A., & Rosolowsky, E. 2013, *ApJ*, 770, 141
 Burkhart, B. 2018, arXiv:1801.05428
 Burkhart, B., Lazarian, A., Leão, I. C., de Medeiros, J. R., & Esquivel, A. 2014, *ApJ*, 790, 130
 Burkhart, B., Collins, D. C., & Lazarian, A. 2015, *ApJ*, 808, 48
 Burkhart, B., Stalpes, K., & Collins, D. C. 2017, *ApJL*, 834, L1
 Burkhart, B., Stanimirović, S., Lazarian, A., & Kowal, G. 2010, *ApJ*, 708, 1204
 Cho, J., & Vishniac, E. T. 2000, *ApJ*, 539, 273
 Cho, J., & Lazarian, A. 2003, *MNRAS*, 345, 325
 Clark, S. E., Hill, J. C., Peek, J. E. G., Putman, M. E., & Babler, B. L. 2015, *Physical Review Letters*, 115, 241302
 Correia, C., Burkhart, B., Lazarian, A., et al. 2014, *ApJL*, 785, L1
 Correia, C., Lazarian, A., Burkhart, B., Pogossyan, D., & De Medeiros, J. R. 2016, *ApJ*, 818, 118
 Crutcher, R. M. 2012, *ARA&A*, 50, 29
 Draine, B. T. 2005, *ESA Special Publication*, 577, 251
 Draine, B. T. 2009, *Cosmic Dust - Near and Far*, 414, 453
 Elmegreen, B. G., & Scalo, J. 2004, *ARA&A*, 42, 211
 Esquivel, A., & Lazarian, A. 2005, *ApJ*, 631, 320
 Esquivel, A., Lazarian, A., Horibe, S., et al. 2007, *MNRAS*, 381, 1733
 Esquivel, A., & Lazarian, A. 2011, *ApJ*, 740, 117
 Esquivel, A., Lazarian, A., & Pogossyan, D. 2015, *ApJ*, 814, 77
 Federrath, C., Chabrier, G., Schober, J., et al. 2011, *Physical Review Letters*, 107, 114504
 Goldreich, P., & Sridhar, S. 1995, *ApJ*, 438, 763
 González-Casanova, D. F., & Lazarian, A. 2017, *ApJ*, 835, 41
 González-Casanova, D. F., Lazarian, A., & Burkhart, B. 2017, arXiv:1703.03035
 González-Casanova, D. F., & Lazarian, A. 2018, in prep
 Haverkorn, M., Gaensler, B. M., McClure-Griffiths, N. M., Dickey, J. M., & Green, A. J. 2006, *ApJS*, 167, 230
 Heyer, M. H., & Brunt, C. 1999, *New Perspectives on the Interstellar Medium*, 168, 387
 Heyer, M., Gong, H., Ostriker, E., & Brunt, C. 2008, *ApJ*, 680, 420-427
 Higdon, J. C. 1984, *ApJ*, 285, 109
 Hu, Y., Yuen, K. H., & Lazarian, A. 2018, arXiv:1802.08772
 Kainulainen, J., & Tan, J. C. 2013, *A&A*, 549, A53
 Kandel, D., Lazarian, A., & Pogossyan, D. 2016, *MNRAS*, 461, 1227
 Kandel, D., Lazarian, A., & Pogossyan, D. 2017, *MNRAS*, 464, 3617
 Kandel, D., Lazarian, A., & Pogossyan, D. 2017, *MNRAS*, 470, 3103
 Krasnopolsky, R., Li, Z.-Y., Shang, H., & Zhao, B. 2012, *ApJ*, 757, 77
 Lazarian, A. 2006, *ApJL*, 645, L25
 Lazarian, A. 2009, *SSRv*, 143, 357
 Lazarian, A., & Pogossyan, D. 2000, *ApJ*, 537, 720
 Lazarian, A., & Vishniac, E. T. 1999, *ApJ*, 517, 700
 Lazarian, A., & Yuen, K. H. 2018, *ApJ*, 853, 96
 Lazarian, A., & Yuen, K. H. 2018, arXiv:1802.00028
 Lazarian, A., Pogossyan, D., & Esquivel, A. 2002, *Seeing Through the Dust: The Detection of HI and the Exploration of the ISM in Galaxies*, 276, 182
 Lazarian, A., Esquivel, A., & Crutcher, R. 2012, *ApJ*, 757, 154
 Lazarian, A., Yuen, K. H., Lee, H., & Cho, J. 2017, *ApJ*, 842, 30
 Mac Low, M.-M., & Klessen, R. S. 2004, *Reviews of Modern Physics*, 76, 125
 Maron, J., & Goldreich, P. 2001, *ApJ*, 554, 1175
 McKee, C. F., & Ostriker, E. C. 2007, *ARA&A*, 45, 565
 Mestel, L., & Spitzer, L., Jr. 1956, *MNRAS*, 116, 503
 Mocz, P., Burkhart, B., Hernquist, L., McKee, C. F., & Springel, V. 2017, *ApJ*, 838, 40
 Montgomery, D., & Mattheaus, W. H. 1995, *ApJ*, 447, 706
 Mouschovias, T. C. 1991, *ApJ*, 373, 169
 Narayan, R., & Medvedev, M. V. 2001, *ApJL*, 562, L129
 Ossenkopf, V. 2002, *A&A*, 391, 295
 Padoan, P., Jimenez, R., Juvela, M., & Nordlund, Å. 2004, *ApJL*, 604, L49
 Roman-Duval, J., Federrath, C., Brunt, C., et al. 2011, *ApJ*, 740, 120
 Schleicher, D. R. G., Banerjee, R., Sur, S., et al. 2010, *A&A*, 522, A115
 Shebalin, J. V., Mattheaus, W. H., & Montgomery, D. 1983, *Journal of Plasma Physics*, 29, 525
 Shu, F. H. 1983, *ApJ*, 273, 202
 Spitzer, L. 1978, *Physical processes in the interstellar medium*, by Lyman Spitzer. New York Wiley-Interscience, 1978. 333 p.,
 Vázquez-Semadeni, E., Banerjee, R., Gómez, G. C., et al. 2011, *MNRAS*, 414, 2511
 Yuen, K. H., & Lazarian, A. 2017, *ApJL*, 837, L24
 Yuen, K. H., & Lazarian, A. 2017, arXiv:1703.03026
 Yuen, K. H., & Lazarian, A. 2018, in prep.
 Yuen, K. H., Lazarian, V., & Lazarian, A. 2018, arXiv:1802.00024

APPENDIX

A. THE FFT OPEN-BOUNDARY CROSS-CORRELATION METHOD

Computationally the cross-correlation function is pretty expensive with computer complexity of $O(N^2)$. This disables scientists to study the statistical behaviour, often force the calculation of anisotropy to be truncated to small scales only. The reason behind is because the usual Fourier Transform method (Eq 8) is not valid in the case when we select partial region for CFA analysis. In the following, based on the formulation from Hockney & Eastwood we explain how one can compute the open boundary problem with similar treatment as in Eq. 7, which facilitates the method of CFA to observational maps and also sub-block studies in parallel of VGT.

In the following treatment we shall interchange integrals $\int dx$ and summation signs \sum_x freely to address the feature that the numerical data (both synthetic and observational) are discrete and having finite resolution.

Assuming we have a piece of complex numerical data $C(r)$ and we would like to obtain its correlation function:

$$CF(r) = \int dr' C^*(r') C(r+r') \quad (\text{A1})$$

where the sign $*$ means complex conjugate. Using the definition of Fourier transform and assuming the functions are all C_2 converging, we have

$$CF(r) = \frac{1}{L^2} \int dr' dk_1 dk_2 C^*(k_1) e^{-ik_1(r'+r)} C(k_2) e^{ik_2 r'} \quad (\text{A2})$$

$$= \frac{1}{L} \int dk C^*(k) C(k) e^{-ikr} \quad (\text{A3})$$

where L is the normalization constant. This formula is essentially Eq 8.

Hockney propose a novel way of tackling the common convolution problem in computational physics especially to tackle Newtonian Gravity using the following implementation, which has been tested in our code in accelerating the open space discrete Poisson calculation from $O(N^2)$ to $O(N \log N)$. Here we follow their idea and calculate the cross-correlation counter-part following the Appendix of Ryne 2011 (arXiv:1111.4971). Suppose one is interested in the discrete cross-correlation

$$f_i = \sum_{j=0}^{n-1} g_j^* h_{i+j} \quad (\text{A4})$$

where $i = 0, 1, 2, \dots, m-1$. Define the zero-pad sequence of g which has the length of $N > m+n$

$$G_j = \begin{cases} g_j, & \text{if } j = 0, 1, 2, \dots, n-1 \\ 0, & \text{if } j = n+1, \dots, N \end{cases} \quad (\text{A5})$$

Similarly, we can define the periodic cross-term

$$H_k = \begin{cases} h_k & \text{if } j = 0, 1, 2, \dots, m+n-1 \\ 0, & \text{if } j = m+n, \dots, N \\ h_{\text{mod}(k, N)}, & \text{otherwise} \end{cases} \quad (\text{A6})$$

The above is the basis the padding strategy as shown in Fig 2.

The analogous summation formula for cross-correlation is similar to Eq. (A4) of Ryne (2011), assuming $W = e^{-2\pi i/N}$

$$F_j = \frac{1}{N} \sum_{k=0}^{N-1} W^{-jk} \left(\sum_{l=0}^{N-1} G_l^* W^{-lk} \right) \left(\sum_{l=0}^{N-1} H_l W^{lk} \right) \quad 1 \leq j \leq N \quad (\text{A7})$$

And we already know Eq. A2 the above formula will provide, in summation form and with the consideration of zero pads in Eq A5:

$$F_i = \sum_{i=0}^{N-1} G_i^* H_j = \sum_{i=0}^{m+n-1} g_i^* h_j \quad (\text{A8})$$

For the specific case that we are interested, $g = h = C$ and having the same size. The minimal number that satisfy the condition $N > m+n \sim 2n$ is $N = 2n+1$. Noticing multidimensional FFT in rectangular case is orthogonal, we therefore arrive with the pictorial description as in Fig 2.

One might question whether the appearance of bad pixels might alter the result we showed in the main text. We therefore perform a simple "hole-punching" test on our existing data. We select a centroid map C from the cube H0 (See Table 2) and randomly set a certain percentage of the pixels to be NaN. We then *directly* use the open-boundary FFT method on the centroid map with different block size to see whether the detected CFA orientation and axis ratio are changed after we zero the NaN pixels. Fig A1 shows the change of axis ratio and orientation when we set a certain percentage of the data to be NaN and then perform CFA using the open-boundary FFT method. We see that even 40% of the data is punch out we still have approximately the same predictions on the axis ratio or major-axis orientation, which suggested that the current open-boundary FFT method would still be robust to real data which will usually carry a number of empty pixels.

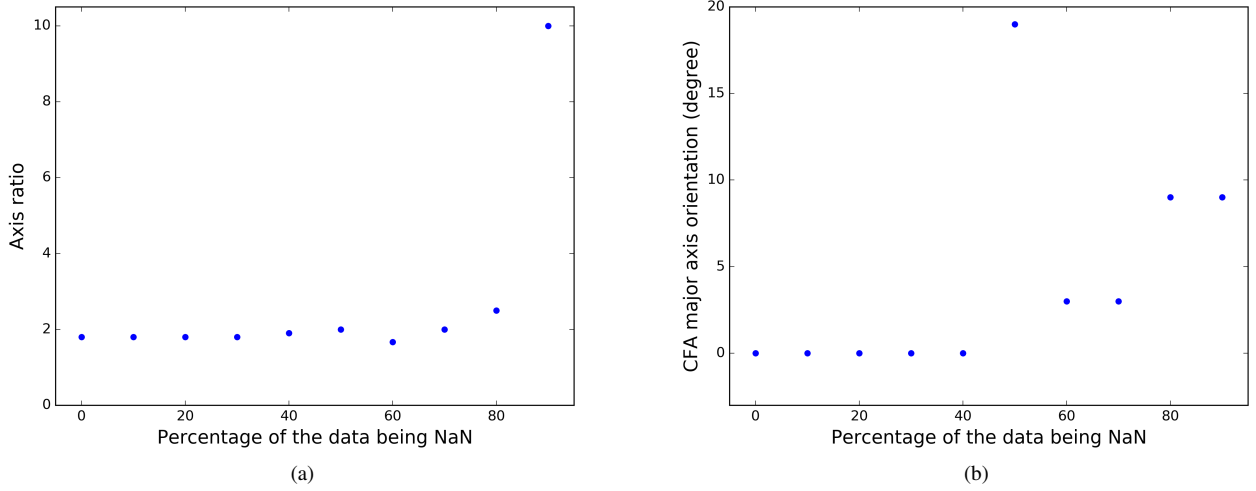


Figure A1. Two panels showing the variance of axis ratio (a/b, left) and orientation of magnetic field as predicted by the CFA (right) when a certain percent of data is set to be NaN.

B. ANISOTROPY

A correct anisotropy can be revealed in a local frame of reference, which is defined with respect to the local mean magnetic field. However, it is possible to observe a (fake) scale-dependent anisotropy in the global frame of reference, which is aligned with the mean magnetic field. For the sake of simplicity, we assume driving is isotropic throughout this Appendix.

If turbulence is sub-Alfvénic, it is easy to understand why we observe a (fake) scale-dependent anisotropy in the global frame of reference. First, we note that large-scale structures are isotropic because driving is isotropic. Second, we note that structures measured in the global frame of reference are anisotropic on very small scales due to field-line wandering on large scales. The anisotropy in the global frame of reference is scale-independent on very small scales and of order $l_{\parallel}/l_{\perp} \sim B_0/b_l \sim 1/M_A$, where l_{\parallel} and l_{\perp} are parallel and perpendicular size of eddies, respectively, and M_A is the Alfvén Mach number. Third, since large scale structures are isotropic and very small-scale ones are anisotropic, there should be transition scales, on which anisotropy is scale-dependent. Note that the scale-dependent anisotropy on the transition scales in the global frame of reference is different from the true anisotropy that can be revealed in a local frame of reference.

Even if $b_L/B_0 \sim M_A \sim 1$, we can have a (fake) scale-dependent anisotropy near the energy injection scale L in the global frame of reference. Suppose that we try to reveal anisotropy using the second-order structure function

$$\mathbf{SF}_2(r_{\perp}, r_{\parallel}) = \langle |\mathbf{A}(\mathbf{x} + \mathbf{r}) - \mathbf{A}(\mathbf{x})|^2 \rangle_{\text{avg. over } \mathbf{x}}, \quad (\text{B9})$$

where \mathbf{A} can be either velocity or magnetic field, r_{\perp} and r_{\parallel} are components of the separation vector \mathbf{r} perpendicular and parallel to the mean magnetic field, respectively. If contours of $\mathbf{SF}_2(r_{\perp}, r_{\parallel})$ are isotropic, we can say structures are isotropic (see Cho & Vishniac 2000). If $b_L/B_0 \sim 1$, we expect that small-scale structures are isotropic and $\mathbf{SF}_2(r_{\perp}, 0) = \mathbf{SF}_2(0, r_{\parallel})$. Note, however, that roughly speaking the second-order structure function represent power near the scale of interest. For example, $\mathbf{SF}_2(r_{\perp}, 0)$ represents power near the (perpendicular) scale r_{\perp} , which is approximately equal to the power in the shaded area in Figure B2(a). Similarly, $\mathbf{SF}_2(r_{\perp}, 0)$ is approximately equal to the power in the shaded area in Figure B2(b). Although we will not show it rigorously, Figure B2 clearly tells us that $\mathbf{SF}_2(r_{\perp}, 0) > \mathbf{SF}_2(0, r_{\parallel})$, which means that structures look anisotropic. The fact that $\mathbf{SF}_2(r_{\perp}, 0) > \mathbf{SF}_2(0, r_{\parallel})$ implies that contours of $\mathbf{SF}_2(r_{\perp}, r_{\parallel})$ are elongated along the direction parallel to the mean magnetic field. Note that this kind of anisotropy appears on sufficiently small scales. Now, the situation is similar to that of sub-Alfvénic turbulence: large scales are isotropic due to isotropic driving and small scales are anisotropic as we have shown above. Therefore, there should be transition scales, on which we observe a (fake) scale-dependent anisotropy.

C. TERM AND ABBREVIATIONS

Table C1. Term and Abbreviation used in the paper.

Abbreviation	Term
AM	Alignment Measure
Continued on next page	

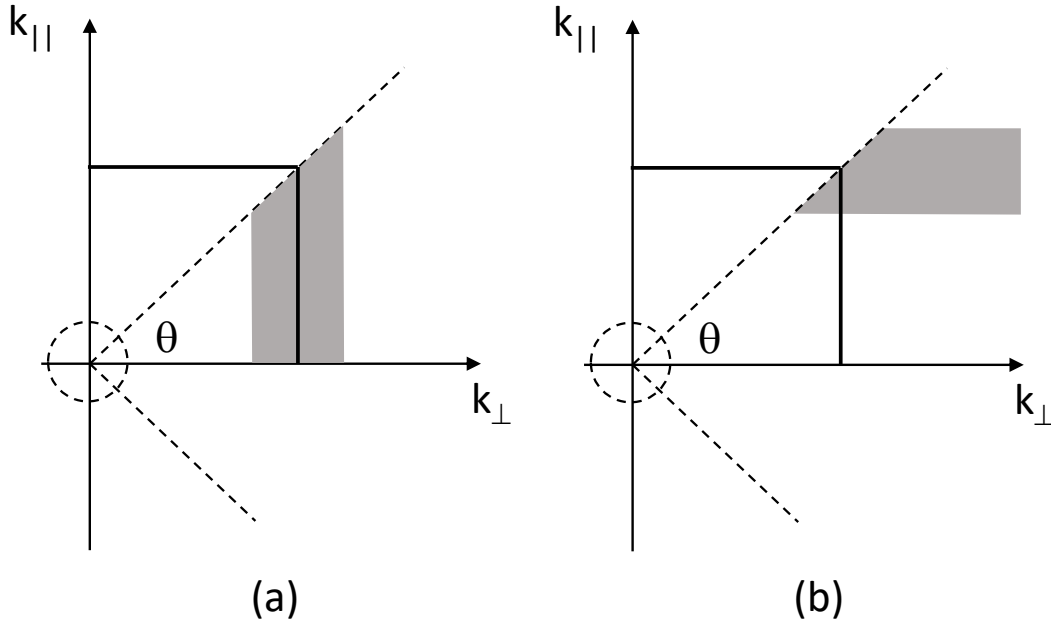


Figure B2. Structure functions for the directions perpendicular ($SF_2(r_{\perp}, 0)$; left panel) and parallel ($SF_2(0, r_{\parallel})$; right panel) to the mean magnetic field. Here $r_{\perp} \propto 1/k_{\perp}$ and $r_{\parallel} \propto 1/k_{\parallel}$.

TABLE C1 – continued from previous page

First column	Second column
ACF	Autocorrelation Function
CFA	Correlation Function Anisotropy
VGT	Velocity Gradient Technique
PCA	Principle Component Analysis
PCAA	Principal Component Analysis of Anisotropies
PPV	Position-Position-Velocity
pPPV	Partial Position-Position-Velocity
pSIG	Polarised Synchrotron Intensity Gradient
VGT	Velocity Gradient Technique
VCG	Velocity Centroid Gradient
MHD	Magneto-hydro-dynamics